molecules

MDPI

Article

A Dual-Function Fe-Doped Co_3O_4 Nanosheet Array for Efficient OER and HER in an Alkaline Medium

Yibo Su [1], Bo Liu [1], Zijun Shi [2], Mei Yan [1] and Tengfei Ma [1,*]

[1] School of Chemistry and Chemical Engineering, Inner Mongolia University of Science & Technology, Baotou 014010, China
[2] Bureau of Science & Technology Talent, Ordos High-Tech Industrial Development Zone, Ordos 017000, China
* Correspondence: matf@mail.nankai.edu.cn

Abstract: The electrocatalysts of heteroatom-doped non-precious metal oxide materials are of great significance for efficient and low-cost electrochemical water-splitting systems. Herein, an innovative Fe-doped Co_3O_4 nanoflake (Fe-Co_3O_4/NF) on nickel foam has been developed, which exhibits excellent electrocatalytic activity for both hydrogen evolution reactions (HERs) and oxygen evolution reactions (OERs). Benefiting from the synergy of the charge redistribution and d-band center shift caused by doping engineering, the as-obtained Fe-Co_3O_4/NF shows both excellent HER (η_{10} = 196 mV) and OER (η_{10} = 290 mV) activities with low Tafel slopes (109 mV dec^{-1} for HER and 49 mV dec^{-1} for OER, respectively) and excellent stability. This work provides an effective method for designing and synthesizing bifunctional electrocatalysts with high activity and stability of metal oxide hybrids for the HER/OER.

Keywords: electrocatalysis; oxygen evolution reaction (OER); Ni foam; hydrogen evolution reactions (HER); d-band center shift

check for updates

Academic Editor: César Augusto Correia de Sequeira

Received: 15 January 2025
Revised: 22 February 2025
Accepted: 23 February 2025
Published: 25 February 2025

Citation: Su, Y.; Liu, B.; Shi, Z.; Yan, M.; Ma, T. A Dual-Function Fe-Doped Co_3O_4 Nanosheet Array for Efficient OER and HER in an Alkaline Medium. *Molecules* **2025**, *30*, 1046. https://doi.org/10.3390/molecules30051046

Copyright: © 2025 by the authors. Licensee MDPI, Basel, Switzerland. This article is an open access article distributed under the terms and conditions of the Creative Commons Attribution (CC BY) license (https://creativecommons.org/licenses/by/4.0/).

1. Introduction

With the increasingly severe global energy crisis and environmental pollution problems, finding efficient and clean renewable energy has become an urgent task. Therefore, hydrogen energy has attracted much attention due to its advantages such as high energy density and zero emissions, and is regarded as an important part of the future energy system [1–3]. Alkaline water electrolysis for hydrogen production technology, as a mature hydrogen production method, has the characteristics of simple operation, low cost, and environmental friendliness, and occupies an important position in the hydrogen energy industry chain [4–6]. However, the traditional alkaline water electrolysis technology has problems such as high energy consumption and low efficiency, which limit its large-scale application. Therefore, the development of efficient and stable electrocatalysts is the key to improving the efficiency of alkaline water electrolysis for hydrogen production [7–9].

Nickel foam (NF), as a three-dimensional porous material, has a high specific surface area, good electrical conductivity, and excellent chemical stability, and is an ideal electrode material [10–12]. And cobalt oxide (Co_3O_4), as a transition metal oxide, shows great potential in the field of electrocatalysis due to its good catalytic activity and low cost [13–15]. Through in situ growth technology, Co_3O_4 nanostructures can be directly formed on the surface of NF, avoiding the material transfer or composite interface problems that may occur in the traditional preparation methods. This integrated design not only simplifies the preparation process, but also greatly improves the stability and durability of the electrode due to the tight combination between the nanostructure and the substrate [16–20]. In

addition, the in situ grown Co_3O_4 nanostructures usually have a higher specific surface area and more active sites, which are crucial for improving the catalytic efficiency of water electrolysis for hydrogen production [21].

Although Co_3O_4 in situ grown on NF shows good catalytic performance in hydrogen production, stability remains an urgent problem to be solved [22]. After working for a long time, Co_3O_4 may fall off or undergo phase transformation, which will result in a decrease or even failure of catalytic activity [23–25]. To improve its stability, researchers have adopted various strategies, such as introducing doping elements and optimizing the preparation process [26–28]. Pan et al. proposed a strategy of synergistically improving catalytic activity through Er doping to enhance the intrinsic activity of OER and the stability of Co_3O_4. At 10 mA cm^{-2}, the overpotential of the Er-Co_3O_4 catalyst with an Er content of 4% is 321 $\pm$ 5 mV, and the stability is significantly improved for more than 250 h [13]. Jiang et al. designed Co-Mn bimetallic nanowires of Co_3S_4/Mn_3O_4 and Co_2P/MnP. The interfacial interaction of Co_3S_4/Mn_3O_4 changes the electronic structure of Co_3S_4, partially fills the oxygen vacancies of Mn_3O_4, and effectively promotes the stability of OER under alkaline conditions. Adding Mn_3O_4 and MnP to modulate Co_3S_4 and Co_2P can reduce the overpotential and extend the stability of the electrolytic water reaction [29]. Except for the problem of stability, another key challenge is the slow reaction kinetics, which mainly includes two aspects, the slow electron transfer rate, and the blocked mass transfer. Researchers proposed methods of optimizing the microstructure of Co_3O_4 by adjusting the preparation conditions and introducing the synergistic effect between bimetals through doping heteroatom to solve the problems. Wang et al. used ZIF-67 as the precursor and template to prepare a series of defect-rich N-doped Co_3O_4/C porous nano cube catalysts (N-Co_3O_4@NC) through a controllable N doping technique. The introduction of N atoms can optimize the electronic structure of Co atoms, resulting in a decrease in the electron density around Co and the formation of N-containing catalytic active sites. Moreover, the N doping and substitution of lattice O in Co_3O_4 will inevitably lead to the formation of oxygen vacancies, which will effectively improve the conductivity of the electrocatalyst [30]. It is worth noting that the difference in the radius between the heteroatom and Co atom may cause lattice distortion or lattice defects in Co_3O_4, which promotes the redistribution of electrons at the two-phase interface, optimizes the adsorption and transformation of active sites to reaction intermediates, increases the electrical conductivity, and improves the catalytic activity.

In this work, a simple in situ hydrothermal synthesis method was employed to prepare flower-like Fe-Co_3O_4/NF as a bifunctional electrocatalyst for HER and OER. Firstly, the flower-like Co_3O_4 was in situ grown on the conductive substrate NF, which possesses a high specific surface area and a large number of active sites. Then, the thickness of the Co_3O_4 nanosheets was altered by doping of the Fe atom, which is beneficial for improving the structural stability of the composite electrocatalyst. Simultaneously, Fe doping effectively regulates the electronic structure of the active center and promotes the redistribution of charges. Moreover, the upward shift of the d-band center caused by the doping engineering enhances the adsorption ability of the electrocatalyst surface to the reaction radicals, thereby improving the HER and OER activities. Fe-Co_3O_4/NF exhibits excellent HER performance (overpotential of 196 mV @ 10 mA cm^{-2}) and OER performance (overpotential of 290 mV @ 10 mA cm^{-2}) in the 1 M KOH electrolyte solution, and can maintain stability for 200 h in 1 M KOH.

2. Results and Discussion

2.1. Morphologic and Composition Characterization

Fe-Co_3O_4/NF-integrated electrocatalyst was synthesized by two steps of a simple hydrothermal reaction and calcination oxidation process (Figure 1a). Firstly, a bimetallic FeCo precursor/NF with a nanosheet morphology was grown on an NF substrate via a simple solvothermal method. Subsequently, the obtained FeCo precursor/NF was calcined in air at 350 °C for 2 h to prepare the final Fe-Co_3O_4/NF. For comparison, Co_3O_4/NF integrated catalyst was prepared using the same synthesis method just without the Fe precursor.

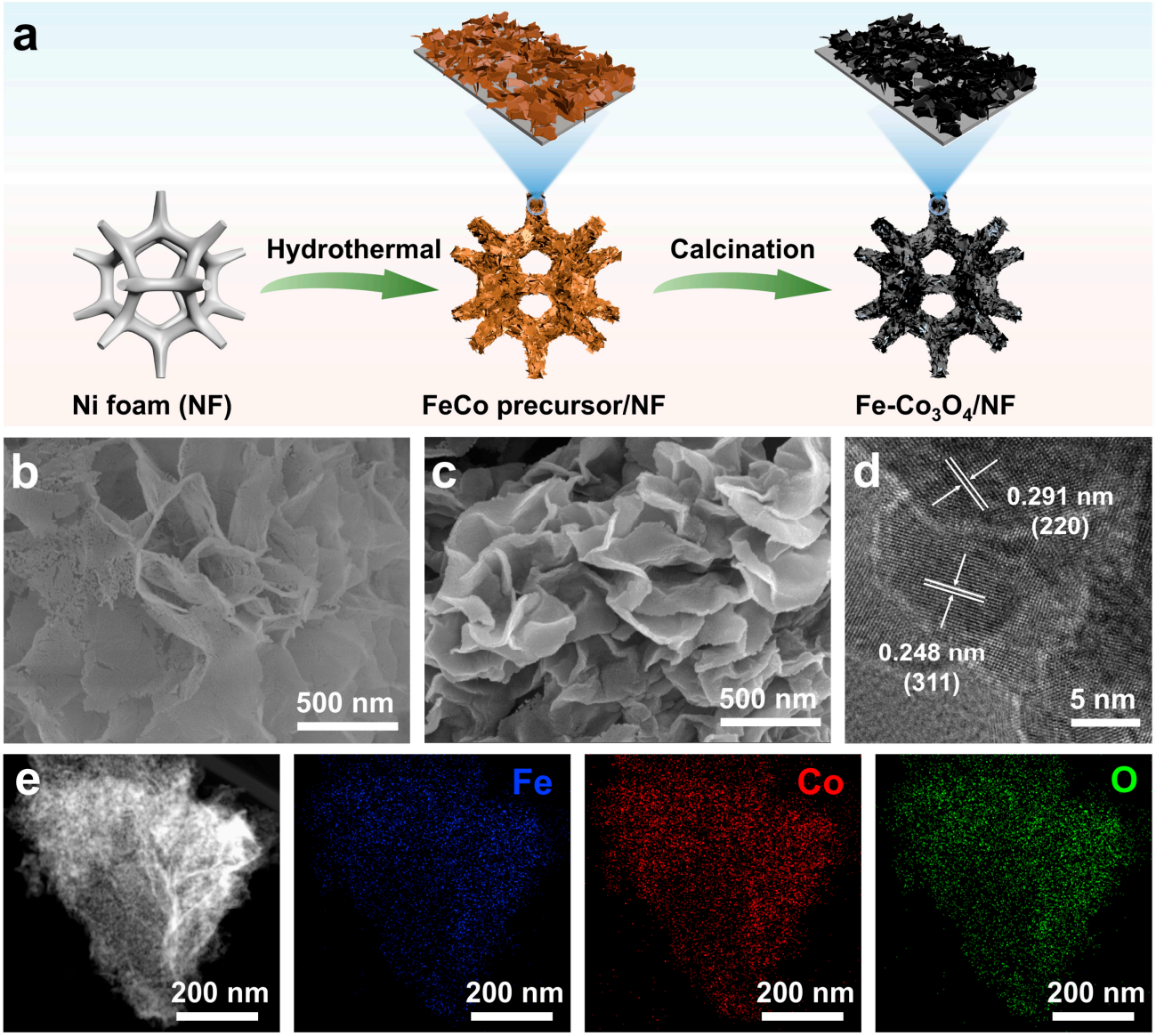


Figure 1. (**a**) Schematic illustration of the synthesis of Fe-Co_3O_4/NF. SEM images of (**b**) Co_3O_4/NF and (**c**) Fe-Co_3O_4/NF. (**d**) TEM image of Fe-Co_3O_4/NF. (**e**) The EDS mapping images of Fe, Co, and O.

The microstructure of the samples was analyzed by scanning electron microscopy (SEM) and transmission electron microscopy (TEM). As shown in Figure S1a, Co_3O_4/NF exhibits a layered nanoflower structure, and it is further observed from Figure 1b that the lamellar structure is assembled from nanoparticles. After doping with Fe, Fe-Co_3O_4/NF still maintains a similar layered nanoflower structure to Co_3O_4/NF, but the thickness of the

lamellae increases significantly, which is beneficial to improving the stability of the catalyst in the reaction process (Figure S1b and Figure 1c).

It is further confirmed by transmission electron microscopy (TEM) that the lamellar structure in the powder sample obtained by ultrasonication of the prepared Fe-Co_3O_4/NF is composed of nanoparticles (Figure 1d), which is consistent with the result of SEM. Further measurement and analysis of its lattice show that the lattice spacings of 0.291 nm and 0.248 nm correspond to the (220) and (311) crystal planes of Co_3O_4, respectively. Compared with the corresponding Co_3O_4 (0.286 nm and 0.244 nm of (220) and (311), JCPDS No.42-1467), the lattice spacing exhibits a slight expansion after the doping of Fe, which proves the successful introduction of Fe in Fe-Co_3O_4/NF. The EDX mapping image in Figure 1e indicates that the Fe, Co, and O elements are uniformly distributed on Fe-Co_3O_4, also indicating that the Fe species have been successfully introduced into the sample.

To investigate the structure of the catalyst, X-ray diffraction (XRD) tests were conducted on the prepared catalysts. As shown in Figure 2a, Fe-Co_3O_4/NF has almost the same diffraction peaks as Co_3O_4/NF (JCPDS No. 42-1467), mainly corresponding to the (220), (311), (511), and (440) crystal planes of Co_3O_4. After doping with Fe species, no characteristic peaks of Fe and its related compounds are formed. However, compared with Co_3O_4/NF, the characteristic diffraction peaks of Fe-Co_3O_4/NF shift to a small angle, which indicates that the doping of Fe will cause the lattice expansion of Co_3O_4 (which consists of the TEM results).

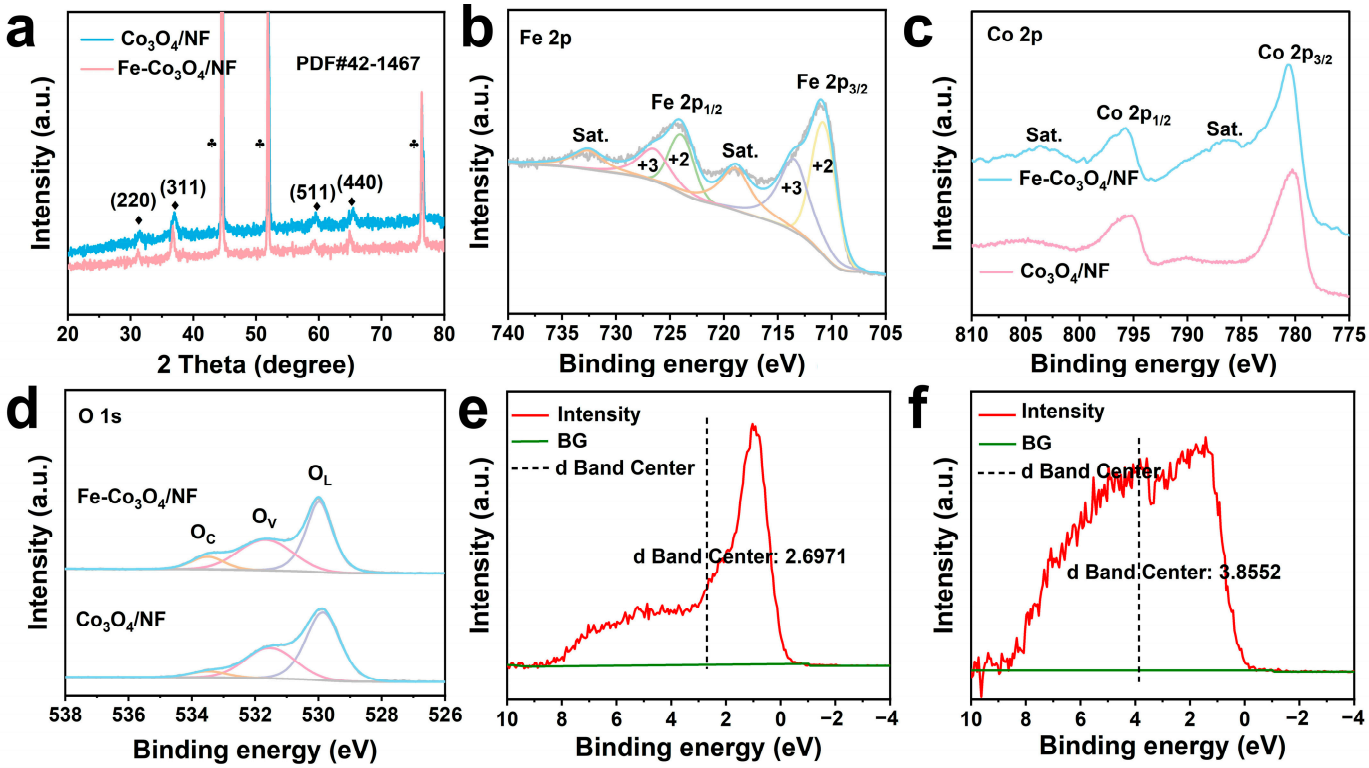


Figure 2. Structural and compositional characterization of the as-prepared samples. (**a**) XRD patterns. High-resolution XPS spectra of (**b**) Fe 2p, (**c**) Co 2p, and (**d**) O 1s. The d-band center position was obtained from the valence-band spectra of (**e**) Co_3O_4/NF and (**f**) Fe-Co_3O_4/NF.

To further explore the changes caused by the doping of Fe, the elemental composition and chemical state of Co_3O_4/NF and Fe-Co_3O_4/NF were analyzed using XPS. The high-resolution Fe 2p spectrum of Fe-Co_3O_4/NF shows two corresponding satellite peaks at 718.89 eV and 732.67 eV (Figure 2a). The fitting peaks at 710.9 eV and 723.4 eV are attributed

to Fe^{2+}, while 714.1 eV and 726.7 eV are attributed to Fe^{3+}, indicating the coexistence of Fe^{2+} and Fe^{3+}.

Although XPS cannot directly observe the physical structure of oxygen vacancy, the existence of oxygen vacancy and its related chemical state and electronic structure can be indirectly proved by analyzing the information of peak position, shape, and intensity in XPS spectra. For the spectra of O 1s (Figure 2b), the three peaks from high binding energy to low binding energy correspond to chemisorbed oxygen (O_C), surface oxygen vacancies (O_V), and lattice oxygen (O_L), respectively. The peak area proportions of O_C, O_V, and O_L of Co_3O_4/NF and Fe-Co_3O_4/NF are obtained through the peak fitting. As shown in Table S1, the O_V concentration increases from 35.95% of Co_3O_4/NF to 40.25% of Fe-Co_3O_4/NF, indicating the successful entrance of doping Fe in the crystal lattice of Co_3O_4, formatting the oxygen vacancies, which facilitates electron conduction and ion transportation.

The Co 2p XPS spectrum of the Co_3O_4/NF (Figure 2c) shows two peaks at 780.23 eV and 795.21 eV belonging to Co $2p_{3/2}$ and Co $2p_{1/2}$, respectively. Compared with the Co_3O_4/NF, the binding energy of Co $2p_{3/2}$ in Fe-Co_3O_4/NF shifts 0.35 eV, indicating that the electron cloud density around Co reduces due to the influence of the doping atom Fe. The introduction of Fe alters the electronic structure of Co_3O_4, increases the unpaired electrons, leads to a stronger electron correlation effect, and causes a charge redistribution between Co and O atoms, enhancing the electron–electron interaction, thereby strengthening the satellite peaks.

It is well known that the position of the d-band center is directly related to the adsorption energy of the intermediate. This is because the change in the adsorption energy of various intermediates to different metals determines the activity and stability of the electrocatalyst, so the d-band center is an important indicator of HER and OER performance [31]. The approximate d-band center position can be obtained from the valence-band spectra [32]. As shown in Figure 2e,f, the d-band center of Fe-Co_3O_4/NF is approximately 1.16 eV higher than that of Co_3O_4/NF. According to the d-band center theory, the increase in the d-band center energy level enhances the adsorption ability of the catalyst surface to the reactive free radicals, which theoretically can improve the activities of HER and OER.

2.2. HER Electrocatalytic Performance

The electrocatalytic HER performance of NF, Co_3O_4/NF, and Fe-Co_3O_4/NF was tested in a 1.0 M KOH electrolyte using a typical three-electrode system. As presented in Figure 3a,b, polarization curves are obtained by LSV with a scanning rate of 2 mV s^{-1}. The Fe-Co_3O_4/NF shows a remarkable catalytic HER activity with a much lower η_{10} of only 196 mV than Co_3O_4/NF (η_{10} = 208 mV) and bare NF (η_{10} = 240 mV). It is worth noting that at 50 mA cm^{-2} high current density, the overpotential required for Fe-Co_3O_4/NF is also lower than that for Co_3O_4 and NF. Moreover, the Fe-Co_3O_4/NF exhibits favorable HER kinetics with a Tafel slope of 109 mV dec^{-1}, which is smaller than that of Co_3O_4 (162 mV dec^{-1}) and NF (189 mV dec^{-1}) (Figure 3c). When the electrode reaction is strongly affected by the diffusion process, such as when the diffusion rate of reactants or products near the electrode surface is slow and cannot be supplemented or removed in time, it will lead to the deviation of the relationship between the current density and the electrode potential from the ideal situation and increase the Tafel slope, which even may exceed 120 mv/dec. EIS measurements reflect the reaction kinetics and conductivity of the catalyst in the HER process, and the fitted Nyquist diagram is shown in Figure 3d. Fe-Co_3O_4/NF exhibits the smallest charge transfer resistance, demonstrating its desirable reaction kinetics and excellent electrical conductivity. In addition, CV curves for the non-faraday region (Figure S2) are collected to determine the C_{dl} (Figure 3e, relative to the RHE). The Fe-Co_3O_4/NF possesses a C_{dl} of 7.06 mF cm^{-2}, significantly higher than those of Co_3O_4/NF

(1.05 mF cm^{-2}) and NF (1.1 mF cm^{-2}), indicating the exposure of more active sites. Moreover, the stability of the catalyst is also important for practical applications. The durability of the electrocatalysts was assessed using current–time (i–t) chronoamperometric measurement. As shown in Figure 3f, the current density of Fe-Co_3O_4/NF at 27.5 mA cm^{-2} exhibits a negligible change during continuous operation over 200 h. The polarization curves also show the same result before and after the 1000-cycle voltammetry cycles (Figure S3).

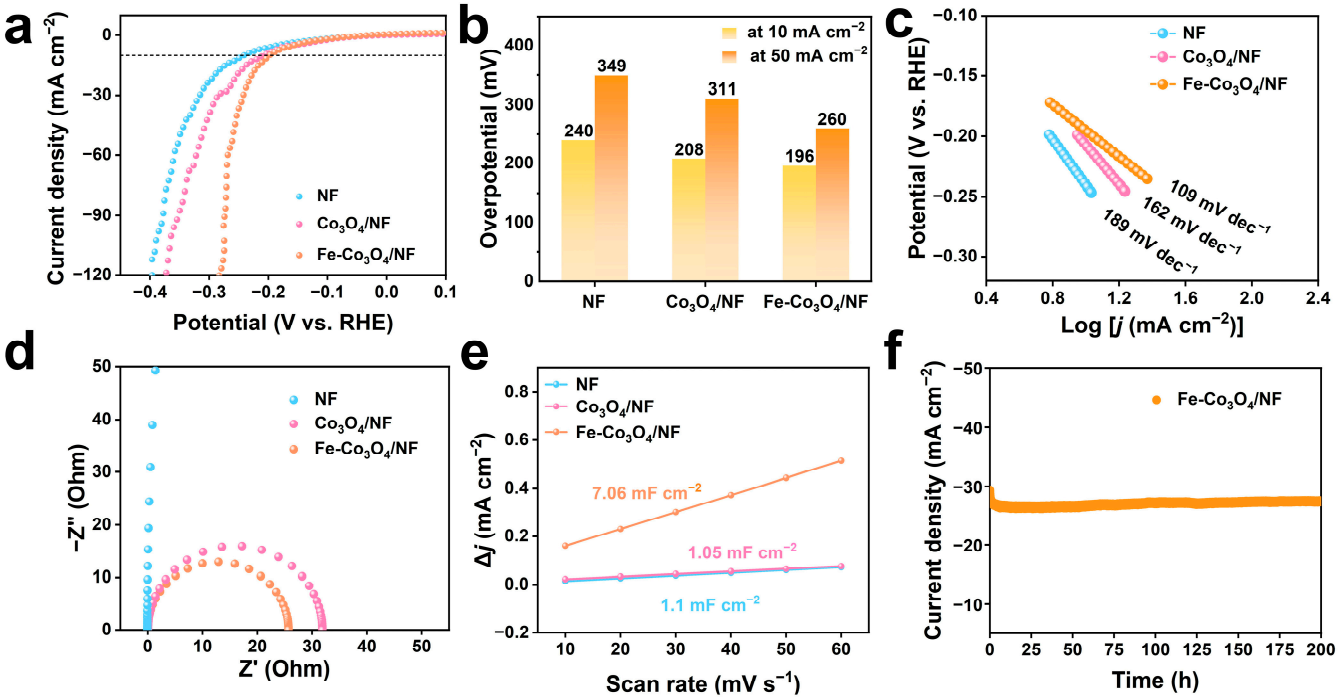


Figure 3. Electrochemical tests of Fe-Co_3O_4/NF and other catalysts for HER in 1 M KOH solution. (**a**) The LSV polarization curves at a scan rate of 2 mV s^{-1}. (**b**) Overpotential at 10 and 50 mA cm^{-2}. (**c**) Tafel plots of various HER electrocatalysts. (**d**) EIS spectra. (**e**) Linear fit of scan rate to capacitive current density of NF, Co_3O_4/NF, and Fe-Co_3O_4/NF. (**f**) The i-t tests performed for various electrocatalysts at the current density of 27.5 mA cm^{-2}.

2.3. OER Electrocatalytic Performance

The OER performances of NF, Co_3O_4/NF, and Fe-Co_3O_4/NF catalysts were further investigated under the same test conditions as above. Figure 4a shows the polarization curves of different catalysts with a potential scanning rate of 2 mV s^{-1}. As shown in Figure 4b, the as-prepared Fe-Co_3O_4/NF exhibits outstanding OER activity and only requires an overpotential of 290 mV at 10 mA cm^{-2} and 319 mV at 50 mA cm^{-2}, which is superior to those of Co_3O_4/NF (324 mV and 360 mV) and NF (350 mV and 405 mV). The Fe-Co_3O_4/NF also shows a much smaller Tafel slope (49 mV dec^{-1}) than those of Co_3O_4/NF (69 mV dec^{-1}) and NF (84 mV dec^{-1}), suggesting it has excellent electrochemical water oxidation kinetics (Figure 4c). The Nyquist radius of Fe-Co_3O_4/NF exhibited the lowest impedance compared to the other catalysts, which was favorable for the OER process (Figure 4d). Moreover, CV curves for the non-faraday region (Figure S3) were collected to determine the double-layer capacitance (C_{dl}). Figure 4e shows that the C_{dl} of Fe-Co_3O_4/NF, Co_3O_4/NF, and NF are estimated as 5.33 mF cm^{-2}, 4.83 mF cm^{-2}, and 0.9 mF cm^{-2}, respectively. The changing trend of the C_{dl} value is like the activity sequence, indicating that the electronic structure is significantly optimized after Fe doping, thus achieving enhanced adsorption/desorption performance. The difference in C_{dl} values between HER and OER can be explained by two factors. Firstly, in HER, fewer intermediates and simpler adsorption/desorption make electrode surface double-layer structure changes less complex.

In OER, intermediate adsorption and reaction alter charge distribution and electric field, causing more obvious double-layer changes. Secondly, HER has moderate hydrogen atom adsorption energy and quick gas generation/desorption, keeping a stable double layer. active catalysts of OER form oxygen-rich layers, enhancing charge storage and increasing capacitance. These jointly lead to C_{dl} value differences. In addition, the durability of Fe-Co_3O_4/NF was further assessed at a fixed current density of 10 mA cm^{-2} (Figure 4f). the Fe-Co_3O_4/NF current density decreased by only 5.6% after 200 h of operation, showing excellent durability. Moreover, the polarization curves of Fe-Co_3O_4/NF before and after 1000 CV cycles remained almost invariant (Figure S4), implying a stable OER activity. In addition, the SEM of the catalyst after HER/OER was characterized (Figure S5), and it can be found that the morphology of the sample has slight changes after testing.

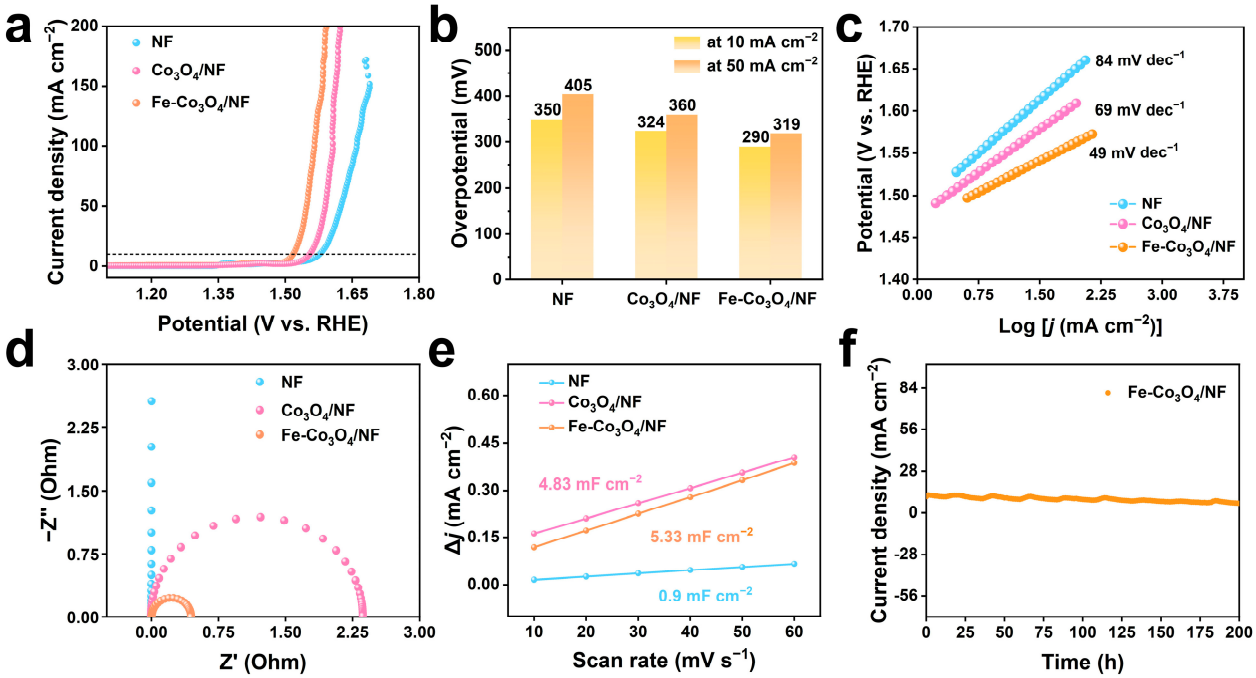


Figure 4. Electrochemical tests of Fe-Co_3O_4/NF and other catalysts for OER in 1 M KOH solution. (**a**) The LSV polarization curves at a scan rate of 2 mV. (**b**) Overpotential at 10 and 50 mA cm^{-2}. (**c**) Tafel plots of various OER electrocatalysts. (**d**) EIS spectra. (**e**) Linear fit of scan rate to capacitive current density of NF, Co_3O_4/NF, and Fe-Co_3O_4/NF. (**f**) The i-t tests performed for various electrocatalysts at the current density of 10 mA cm^{-2}.

In order to explore the role of 2-methylimidazole, the ligand-free samples were prepared and the HER and OER properties were tested. As shown in Figure S6, for HER performance, the sample without ligand preparation is significantly inferior to the previous Fe-Co_3O_4/NF. As for the OER performance, it is also inferior to the sample with a ligand at a higher current density. Therefore, 2-methylimidazole as a ligand coordinates with cobalt ions to form cobalt-based derivatives with unique structures and properties after high-temperature calcination, which is conducive to improving the activity of the catalyst, especially for HER.

To further investigate the influence of Fe salt content on the catalytic performance, in addition to the sample with 0.2 g of iron salt, samples with iron salt contents of 0.1 g and 0.3 g (denoted as 0.1 Fe-Co_3O_4/NF and 0.3 Fe-Co_3O_4/NF, respectively) were prepared, and their catalytic performances were evaluated. As shown in Figure S7, the HER activity of 0.2 Fe-Co_3O_4/NF is significantly superior to that of 0.1 Fe-Co_3O_4/NF and 0.3 Fe-Co_3O_4/NF,

while the OER performance of all three samples is nearly identical. Therefore, 0.2 Fe-Co_3O_4/NF is identified as a more effective catalyst.

3. Materials and Methods

3.1. Materials

Cobalt nitrate hexahydrate ($Co(NO_3)_2 \cdot 6H_2O$, AR, 99%), ferric nitrate nonahydrate ($Fe(NO_3)_3 \cdot 9H_2O$, AR, 98.5%), 2-methylimidazole (2-mim, $C_4H_6N_2$, 98%), and potassium hydroxide (KOH, 95%) were purchased from Macklin Biochemical Technology Co., Ltd., Shanghai, China. Acetone (CH_3COCH_3, AR) and hydrochloric acid (HCl, AR) were purchased from Kelong Chemical Co., Ltd., Chengdu, China. Methanol anhydrous (CH_3OH, AR) and ethanol (C_2H_5OH, AR) were obtained from Kemiou Chemical Reagent Co., Ltd., Tianjin, China. All the reagents and solvents were used without further purification. Nickel foam (NF, 100 × 100 × 1.0 mm) was purchased from Suzhou Astronergy New Material Co., Ltd., Suzhou, China. Deionized (DI) water was homemade.

3.2. Synthesis of Materials

Co_3O_4/NF was in situ synthesized on NF by the hydrothermal method. Typically, a commercial NF was cut into rectangular pieces (3 × 3 cm^2), and, respectively, washed with acetone, and diluted HCl (3 M) for 5 min to remove impurities. Then, the NF was rinsed with ethanol and DI water several times and dried to obtain the cleaned NF for further use.

Firstly, 1.02 g of $Co(NO_3)_2 \cdot 6H_2O$ was dissolved in 15 mL of methanol to form a solution A, and 0.616 g of 2-methylimidazole was dissolved in 15 mL of methanol to form a solution B. Then, a mixture of solution A and solution B was transferred into a 50 mL Teflon-lined stainless-steel autoclave with a piece of vertically inserted cleaned NF and kept at 120 °C for 4 h. After naturally cooling to room temperature, the sample was collected and washed several times with ethanol and water and dried in a vacuum oven at 60 °C for 6 h. The sample was placed in a muffle furnace and calcined in air at 350 °C for 2 h to obtain Co_3O_4/NF.

Firstly, 1.02 g of $Co(NO_3)_2 \cdot 6H_2O$ and 0.202 g of $Fe(NO_3)_3 \cdot 9H_2O$ were dissolved in 15 mL of methanol to form a solution A, 0.616 g of 2-methylimidazole was dissolved in 15 mL of methanol to form a solution B. Then, a mixture of solution A and solution B was transferred into a 50 mL Teflon-lined stainless-steel autoclave with a piece of vertically inserted cleaned NF and kept at 120 °C for 4 h. After natural cooling to room temperature, the sample was collected and washed several times with ethanol and water, and dried in a vacuum oven at 60 °C for 6 h. Finally, the sample was placed in a muffle furnace and calcined in air at 350 °C for 2 h and was labeled as Fe-Co_3O_4/NF.

3.3. Characterization

The structural and compositional information of Co_3O_4/NF and Fe-Co_3O_4/NF were detected by scanning electron microscope (SEM, Zeiss 360 Sigma, Oberkochen, Germany), transmission electron microscopy, high-resolution electron microscopy, and energy-dispersive X-ray spectroscopy mapping with an acceleration voltage of 200 kV (TEM, HRTEM, and EDS-Mapping, JEM-2800, JEOL, Tokyo, Japan). The material microstructure of the samples was examined by X-ray diffractometer (XRD, Rigaku Ultima IV, Tokyo, Japan) from 10° to 90° with a speed of 10° min^{-1}. X-ray photoelectron spectroscopy measurement was used to analyze the surface chemical states of the samples (XPS, ESCALAB 250Xi, Al Kα, Thermo Scientific, Waltham, MA, USA).

3.4. Electrochemical Measurements

Electrochemical tests were performed on the CorrTest electrochemical workstation. The HER and OER properties of the catalyst were tested with a three-electrode system 1 M KOH electrolyte. The samples were directly used as the working electrode, while the graphite rod and Hg/HgO electrode served as counter electrode and reference electrode, respectively. All potential values were calibrated with a reversible hydrogen electrode (RHE) according to the Nernst equation: $E_{RHE} = E_{Hg/HgO} + 0.0592 \times pH + 0.098$. The working electrode was cycled at a scan rate of 50 mV s^{-1} for 30 cycles to activate the electrode in the electrolyte. Linear sweep voltammetry (LSV) measurements were obtained at a sweep rate of 2 mV s^{-1} with 90% iR compensation. The electrical double layer capacitance (C_{dl}) was calculated from cyclic voltammograms (CV) obtained in the non-Faraday interval at scanning rates of 10, 20, 30, 40, 50, and 60 mV s^{-1}. The ECSA can be obtained by the formula ECSA = C_{dl}/C_s. Electrochemical impedance spectroscopy (EIS) was tested in the frequency range of 100 kHz to 0.01 Hz and an AC amplitude of 5 mV. The long-term stability test was measured by chronopotentiometry at a fixed current density of 27.5 mA cm^{-2} (HER) and 10 mA cm^{-2} (OER) for 200 h.

4. Conclusions

In summary, the introduction of Fe heteroatoms into Co_3O_4 by doping engineering was reported to enhance the activity of the HER and OER in alkaline conditions. Impressively, the Fe-Co_3O_4/NF require a low potential of 196 mV to achieve a current density of 10 mA cm^{-2} for the HER and 290 mV to achieve 10 mA cm^{-2} for the OER. The Fe-Co_3O_4/NF towards alkaline HER and OER all exhibited high stability and can maintain a current density of 27.5 mA cm^{-2} and 10 mA cm^{-2} for 200 h, respectively. The experimental results indicated that the essential factor in promoting electrocatalytic performance is due to the charge redistribution and the upward shift of the d-band center caused by Fe doping. This study is of significance for the design and development of highly efficient and stable HER and OER bifunctional electrocatalysts in alkaline media.

Supplementary Materials: The following supporting information can be downloaded at https://www.mdpi.com/article/10.3390/molecules30051046/s1, Figure S1: the photos of NF, FeCo precursor/NF and Fe-Co_3O_4/NF; Figure S2: SEM images of (a) Co_3O_4/NF and (b) Fe-Co_3O_4/NF; Figure S3: HER CV curves of (a) NF, (b) Co_3O_4/NF, (c) Fe-Co_3O_4/NF with different scan rates from 10 to 60 mV s^{-1}, and (d) polarization curves of Fe-Co_3O_4/NF electrode before and after 1000 CV cycles in 1.0 M KOH; Figure S4: OER CV curves of (a) NF, (b) Co_3O_4/NF, (c) Fe-Co_3O_4/NF with different scan rates from 10 to 60 mV s^{-1}, and (d) polarization curves of Fe-Co_3O_4/NF electrode before and after 1000 CV cycles in 1.0 M KOH; Figure S5: SEM images of Fe-Co_3O_4/NF after (a) HER and (b) OER; Figure S6: the LSV polarization curves of Fe-Co_3O_4/NF with and without 2-methylimidazole at a scan rate of 2 mV s^{-1} for (a) HER and (b) OER; Figure S7: the LSV polarization curves of Fe-Co_3O_4/NF with different amount of Fe for (a) HER and (b) OER. Table S1: the calculated OC, OV, and OL proportion from XPS spectra of Co_3O_4/NF and Fe-Co_3O_4/NF.

Author Contributions: Y.S.: conceptualization, methodology, validation, investigation, resources; M.Y.: methodology, validation; Z.S.: investigation, revision; B.L.: writing—review and editing, funding acquisition; T.M.: conceptualization, validation, writing—review and editing, supervision, funding acquisition. All authors have read and agreed to the published version of the manuscript.

Funding: The work was supported by the Natural Science Foundation of the Inner Mongolia Autonomous Region of China (Youth Fund Project, No. 2024QN05012, Inner Mongolia Science and Technology Department), the Basic Scientific Research Business Expenses of Universities Directly Under the Autonomous Region of China (No. 2024QNJS014 and 2024QNJS016, Inner Mongolia University of Science & Technology), and the Scientific Research Support for the Introduction of

High-level Talents by Institutions at the Autonomous Region of China (Inner Mongolia Science and Technology Department).

Institutional Review Board Statement: Not applicable.

Informed Consent Statement: Not applicable.

Data Availability Statement: The data presented in this study are available in the article.

Conflicts of Interest: The authors declare that they have no known competing financial interests or personal relationships that could have appeared to influence the work reported in this paper.

References

1. Wei, C.; Xu, Z.C.J. The possible implications of magnetic field effect on understanding the reactant of water splitting. *Chin. J. Catal.* **2022**, *43*, 148–157. [CrossRef]
2. Li, C.M.; Yu, G.T.; Shen, X.P.; Li, Y.; Chen, W. Theoretical study on the high HER/OER electrocatalytic activities of 2D GeSi, SnSi, and SnGe monolayers and further improvement by imposing biaxial strain or doping heteroatoms. *Molecules* **2022**, *27*, 5092. [CrossRef]
3. Hao, M.H.; Shen, D.C.; Li, Q.; Xiao, Z.T.; Liu, L.C.; Li, C.H.; Wang, W.T. The combination of hydrogen evolution, nitric oxide oxidation and Zn-nitrate battery for energy conversion and storage by an efficient nitrogen-dopped CoO_X electrocatalyst with Turing structure. *J. Colloid Interface Sci.* **2025**, *683*, 477–488. [CrossRef]
4. Jia, H.L.; Wang, H.Y.; Yan, F.F.; Li, Z.; Li, R.J.; Li, S.S.; Wang, J.J.; Zhang, H.C. Fe dimers incorporated within $Ni(OH)_2$ nanosheets to enable rapid oxygen radical coupling and exceptional durability in oxygen evolution. *Appl. Catal. B Environ.* **2025**, *364*, 124861. [CrossRef]
5. Germano, L.D.; De Angelis, L.D.; Batista, A.P.D.; De Oliveira-Filho, A.G.S.; De Torresi, S.I.C. Plasmon enhanced oxygen evolution reaction on Au decorated $Ni(OH)_2$ nanostructures: The role of alkaline cations solvation. *Appl. Catal. B Environ.* **2025**, *363*, 124804. [CrossRef]
6. Xu, N.; Li, M.M.; Sun, H.Y.; Li, G.D.; Wen, X.; Ouyang, D.H.; Liu, C.Y.; Chai, Y.M.; Dong, B. Atmosphere-driven oriental regulation of Ru valence for boosting alkaline water electrolysis. *Chem. Eng. J.* **2024**, *502*, 158051. [CrossRef]
7. Liu, W.; Wang, F.; Wang, A.Y.; Guo, Y.Z.; Yin, H.Y.; Wang, D.H. Boosting alkaline hydrogen evolution reaction by modulating d-band center in bimetallic sulfide Ni_3S_2-FeS heterointerfaces. *Small* **2024**, *21*, 2411028. [CrossRef]
8. Li, D.Q.; Chen, M.P.; Liu, D.; Shen, C.C.; Sun, H.C.; Zhang, Y.X.; He, T.W.; Lu, Q.J.; Li, B.; Zhou, T.; et al. Engineering ruthenium species on metal-organic frameworks for water electrolysis at industrial current densities. *Adv. Energy Mater.* **2024**, *15*, 2404714. [CrossRef]
9. Kuczynski, M.; Mikolajczyk, T.; Pierozynski, B.; Bramowicz, M.; Kulesza, S. An impact of prolonged electrolysis on the electrochemical performance and surface characteristics of NiFe-modified graphite electrodes for alkaline water electrolysis. *Molecules* **2024**, *29*, 5820. [CrossRef]
10. Tang, Y.; Fan, C.Y.; Zang, Z.H.; Cheng, Y.H.; Li, L.L.; Yu, X.F.; Yang, X.J.; Lu, Z.M.; Zhang, X.H.; Liu, H. Non-metallic surface-modified X-Cu (X = F, Cl, Br) metal catalysts for all-pH hydrogen evolution reaction with high performance. *J. Colloid Interface Sci.* **2025**, *683*, 312–321. [CrossRef]
11. Du, H.F.; He, S.; Li, B.X.; Wang, K.; Zhou, Z.K.; Li, J.H.; Wang, T.F.; Du, Z.Z.; Ai, W.; Huang, W. Cascade reaction enables heterointerfaces-enriched nanoarrays for ampere-level hydrogen production. *Angew. Chem. Int. Ed.* **2024**, *137*, e202422393. [CrossRef]
12. Kalaiyarasan, G.; Lee, D.; Lee, J.W.; Ko, M.J. Electrochemical synthesis of nickel hexacyanoferrate and nickel sulfide on nickel foam as sustainable electrocatalysts for hydrogen generation via urea electrolysis. *ACS Appl. Mater. Interfaces* **2024**, *16*, 69142–69152. [CrossRef]
13. Pan, S.J.; Li, H.; Wang, T.Y.; Fu, Y.; Wang, S.N.; Xie, Z.S.; Wei, L.; Li, H.; Li, N. Er-doping enhances the oxygen evolution performance of cobalt oxide in acidic medium. *ACS Catal.* **2024**, *14*, 13814–13824. [CrossRef]
14. Feng, Y.; Li, Z.; Cheng, C.Q.; Kang, W.J.; Mao, J.; Shen, G.R.; Yang, J.; Dong, C.K.; Liu, H.; Du, X.W. Strawberry-like Co_3O_4-Ag bifunctional catalyst for overall water splitting. *Appl. Catal. B Environ.* **2021**, *299*, 120658. [CrossRef]
15. Ajmal, S.; Rasheed, A.; Sheng, W.X.; Dastgeer, G.; Nguyen, Q.A.T.; Wang, P.H.; Chen, P.; Liu, S.J.; Bui, V.Q.; Zhu, M.Z.; et al. Synergetic modulation of electronic properties of cobalt oxide via "Tb" single atom for uphill urea and water electrolysis. *Adv. Mater.* **2024**, *37*, 2412173. [CrossRef] [PubMed]
16. Duan, F.; Huang, Y.J.; Han, T.; Jia, B.; Zhou, X.; Zhou, Y.; Yang, Y.W.; Wei, X.J.; Ke, G.L.; He, H.C. Enhanced oxygen evolution reaction performance on NiS_x@Co_3O_4/nickel foam electrocatalysts with their photothermal property. *Inorg. Chem.* **2023**, *62*, 12119–12129. [CrossRef]

17. Tian, L.; Zhong, D.Z.; Zhao, T.; Liu, Y.; Hao, L.; Fang, Q.; Lang, X.L.; Zhao, X.; Hao, G.Y.; Liu, G.; et al. Oxygen-vacancy-rich Co_3O_4@Fe-B-O heterostructure for efficient oxygen evolution reaction in alkaline and neutral media. *J. Colloid Interface Sci.* **2023**, *646*, 452–460. [CrossRef] [PubMed]
18. Wang, X.Y.; Xiang, R.; Li, S.; Song, K.J.; Huang, W.Z. Self-standing 2D/2D Co_3O_4@FeOOH nanosheet arrays as promising catalysts for the oxygen evolution reaction. *Dalton Trans.* **2023**, *52*, 2002–2012. [CrossRef]
19. Zhang, L.; Lin, B.W.; Ye, S.Z.; Chen, S.Q.; Yao, Z.Q.; Lin, J.C.; Lin, X.; Guo, C.L.; He, J.Y.; Chen, Y.Y.; et al. Controllable disorder engineering in Mn-doped Co_3O_4/NF electrocatalyst for efficient overall water-splitting. *J. Alloys Compd.* **2023**, *956*, 170218. [CrossRef]
20. Xi, Z.W.; Zhou, H.Y.; Liu, Y.X.; Xu, C.L. CuO-Co_3O_4 nanoparticle catalysts rich in oxygen vacancies toward upgrading anodic electro-oxidation of glycerol. *Electrochim. Acta* **2023**, *470*, 143285. [CrossRef]
21. Alhakemy, A.Z.; Senthilkumar, N.; Ding, Y.C.; Li, J.W.; Wen, Z.H. Co_3O_4–C@FeMoP on nickel foam as bifunctional electrocatalytic electrode for high-performance alkaline water splitting. *Int. J. Hydrogen Energy* **2021**, *46*, 32846–32857. [CrossRef]
22. Wang, Z.C.; Liu, H.L.; Ge, R.X.; Ren, X.; Ren, J.; Yang, D.J.; Zhang, L.X.; Sun, X.P. Phosphorus-doped Co_3O_4 nanowire array: A highly efficient bifunctional electrocatalyst for overall water splitting. *ACS Catal.* **2018**, *8*, 2236–2241. [CrossRef]
23. Liu, L.; Ou, Y.Q.; Sun, D. Activity and stability of CoM_xO_y/Co_3O_4 (M = Mo, W, V) nano-arrays synthesized by self-templated method for water oxidization. *Chem. Eng. J.* **2021**, *426*, 130063. [CrossRef]
24. Tao, Y.T.; Wu, J.; Peng, C.; Qiao, S.K.; Song, Y.B.; Peng, L.; Chen, J.; Zhang, H.; Wang, Z.Y.; Lin, J. Pine needle-like FeCo@C grown in situ on nickel foam to enhance the oxygen evolution reaction. *Int. J. Hydrogen Energy* **2023**, *48*, 35112–35122. [CrossRef]
25. Guo, B.S.; Bian, Q.N.; Tan, D.X.; Zhang, D.; Kong, Q.K.; Feng, Y.Y. CoFe$(OH)_x$-Co_3O_4/NF as highly efficient electrocatalyst for oxygen evolution and urea oxidation reactions at high current densities. *J. Alloys Compd.* **2024**, *994*, 174706. [CrossRef]
26. Yuan, H.F.; Wang, S.M.; Ma, Z.Z.; Kundu, M.; Tang, B.; Li, J.P.; Wang, X.G. Oxygen vacancies engineered self-supported B doped Co_3O_4 nanowires as an efficient multifunctional catalyst for electrochemical water splitting and hydrolysis of sodium borohydride. *Chem. Eng. J.* **2021**, *404*, 126474. [CrossRef]
27. Li, J.; Lv, Y.; Wu, X.; Xue, R.; Yang, Z.; Guo, J.; Jia, D. Electronic and vacancy engineering of ruthenium doped hollow-structured NiO/Co_3O_4 nanoreactors for low-barrier electrochemical urea-assisted energy-saving hydrogen production. *J. Colloid Interface Sci.* **2024**, *683*, 600–611. [CrossRef]
28. Hu, X.R.; Zhang, M.M.; Lai, C.; Cheng, M.; Xu, F.H.; Ma, D.S.; Li, L.; Yan, H.C.; Sun, H.; Fan, X.; et al. Metal-organic frameworks derived low-cost Cu-doped Co_3O_4 for efficient reduction of ultra-low nitrate concentrations to ammonia. *Chem. Eng. J.* **2024**, *493*, 152543. [CrossRef]
29. Jiang, Y.; Song, Z.; Qu, M.; Jiang, Y.; Luo, W.; He, R. Co-Mn bimetallic nanowires by interfacial modulation with/without vacancy filling as active and durable electrocatalysts for water splitting. *Small* **2024**, *20*, 2400859. [CrossRef] [PubMed]
30. Zhang, S.L.; Guan, B.Y.; Lu, X.F.; Xi, S.; Du, Y.; Lou, X.W. Metal atom-doped Co_3O_4 hierarchical nanoplates for electrocatalytic oxygen evolution. *Adv. Mater.* **2020**, *32*, 2002235. [CrossRef]
31. Wu, X.; Shao, Z.; Zhu, Q.; Hou, X.; Wang, C.; Zeng, J.; Huang, K.; Feng, S. Tuning the d-band center of Co_3O_4 via octahedral and tetrahedral Co doping for oxygen evolution reaction. *ACS Catal.* **2024**, *14*, 5888–5897. [CrossRef]
32. Wang, R.; Qiu, Z.; Wan, S.; Wang, Y.; Liu, Q.; Ding, J.; Zhong, Q. Insight into mechanism of divalent metal cations with different d-bands classification in layered double hydroxides for light-driven CO_2 reduction. *Chem. Eng. J.* **2022**, *427*, 130863. [CrossRef]

Disclaimer/Publisher's Note: The statements, opinions and data contained in all publications are solely those of the individual author(s) and contributor(s) and not of MDPI and/or the editor(s). MDPI and/or the editor(s) disclaim responsibility for any injury to people or property resulting from any ideas, methods, instructions or products referred to in the content.